Article:
Liu, C., Li, Y., Li, W. et al. (10 more authors) (2024) LSPR-enhanced photoresponsive antibacterial efficiency of Bi/MoS2-loaded fibrin gel for management of diabetic wounds. International Journal of Biological Macromolecules, 277 (3). 134430. ISSN 0141-8130

https://doi.org/10.1016/j.ijbiomac.2024.134430

LSPR-enhanced Photoresponsive Antibacterial Efficiency of Bi/MoS_2-loaded Fibrin Gel for Management of Diabetic Wounds

Chengli Liu [a, b, #], Yuman Li [f, #], Wei Li [a, b, #], Youzhun Fan [a, b], Wuyi Zhou [c], Cairong Xiao [a, b], Peng Yu [a, b], Yueyao Liu [a, b], Xiangqian Liu [d], Zhiguang Huang [d], Xuebin Yang [e, *], Chengyun Ning [a, b, *], Zhengao Wang [a, b, c, *]

[a] School of Material Science and Engineering, South China University of Technology, Guangzhou 510641, P.R. China

[b] National Engineering Research Center for Tissue Restoration and Reconstruction, South China University of Technology, Guangzhou 510641, P.R. China

[c] Research Center of Biomass 3D Printing Materials, College of Materials and Energy, South China Agricultural University, Guangzhou 510642, P.R. China

[d] Nox Bellcow Cosmetics Co., Ltd., Zhongshan 528427, P.R. China

[e] Biomaterials and Tissue Engineering Group, School of Dentistry, University of Leeds, Leeds, LS97TF UK

[f] Department of Geriatric Dentistry, Peking University School and Hospital of Stomatology & National Center for Stomatology & National Clinical Research Center for Oral Diseases & National Engineering Research Center of Oral Biomaterials and Digital Medical Devices, Beijing 100081, PR China

[#] These authors contributed equally to this work.

* Corresponding authors. E-mail addresses: zhengao@scut.edu.cn (Z. Wang), imcyning@scut.edu.cn (C. Ning), x.b.yang@leeds.ac.uk (X. Yang).

Abstract

Chronic diabetic wounds present formidable challenges, marked by uncontrolled bacterial infections, prolonged inflammation, and impaired angiogenesis. The evolving landscape of photo-responsive antibacterial therapy holds great promise in addressing these multifaceted issues, with a particular focus on leveraging the distinctive properties of 2D heterojunction materials. In this investigation, we engineered composite sprayed hydrogels, seamlessly integrating Bi/MoS_2 nano-heterojunctions. Capitalizing on the synergistic interplay between photocatalytic antibacterial and photothermal antibacterial mechanisms, the Bi/MoS_2 heterojunction, guided by its localized surface plasmon resonance, demonstrated outstanding antibacterial efficacy within a mere 10-minute exposure to 808 nm near-infrared light. This accelerated sterilization both *in vitro* and *in vivo*, consequently expediting wound healing. The sprayed composite gel not only furnishes protective shielding for skin tissues but also fosters endothelial cell proliferation, vascularization, and angiogenesis. This safe and ultrafast sterilizing hydrogel presents immense potential for application in antimicrobial dressings, thereby offering a promising avenue for diabetic wound healing.

Keywords: nano-heterojunctions, antimicrobial, near-infrared light, diabetic wound repair.

1. Introduction

Bacterial infections present a formidable global health challenge, particularly within the realm of chronic wound healing[1, 2]. Individuals managing diabetes, fraught with blood sugar control complexities, grapple with recurrent bacterial infections in wounds[3]. This impedes blood vessel repair, disrupt the natural healing process and, in severe cases, necessitating amputation[3, 4]. Given the protracted and intricate nature of diabetic wound repair, there is an imperative need for innovative approaches. The predominant method currently employed involves the extended use of antibiotics. However, antibiotic resistance remains an inescapable challenge, and potentially leads to the emergence of superbugs due to antibiotic misuse[5-8]. In recent decades,

nanomaterials, encompassing metal nanoparticles[9, 10], carbon nanomaterials[11], and metal sulfide nanomaterials[12], have surfaced as promising antibacterial agents. While silver nanoparticles have garnered significant attention for their antibacterial properties, concerns over toxicity associated with elevated silver ion concentrations hinder their long-term application[13-15]. Similarly, carbon nanomaterials exhibit notable antibacterial effects, yet their biotoxicity remains a topic of debate, necessitating further exploration into their degradation and elimination during later treatment stages[16]. A noteworthy advancement in recent years is the escalating interest in light-assisted antimicrobial therapy[17-19]. Unlike traditional methods, photo-assisted antibacterial approaches offer broad-spectrum, high-efficiency sterilization without inducing drug resistance[20]. The synergistic integration of photocatalytic antibacterial (PCA) and photothermal antibacterial (PTA) strategies has demonstrated considerable efficacy[20]. However, these approaches yield limited outcomes in diabetic wound management. Despite promising developments in wound autografts, innovative dressings, and tissue engineering products, their full effectiveness in promoting vascularization in diabetic wounds is hindered by the complex microenvironment and the absence of a coordinated treatment design[21-24]. Hence, there is a pressing need for the development of advanced wound repair materials that facilitate angiogenesis, neo-vascularization, and the timely resolution of inflammation and bacterial infections in chronic diabetic wound tissues.

Molybdenum disulfide (MoS_2), a representative metal sulfide, possesses properties such as a direct band gap, high catalytic activity, broad spectral response, and excellent photothermal conversion efficiency, making it a focal point in photocatalysis research[25, 26]. Despite its excellent biocompatibility, the photocatalytic efficiency and antibacterial activity of pure MoS_2 are limited. Recent studies on doping transition metals in nano-MoS_2 to enhance catalytic performance have shown promise[27-29]. In this context, we chose Bi as the catalytic transition metal due to its low carrier density and high electron conductivity, facilitating electron-hole separation and improving the photocatalytic activity of MoS_2. Additionally, the localized surface plasmon resonance

(LSPR) of Bi nanoparticles under near-infrared light irradiation can enhance photocatalytic activity and induce a photothermal effect[30, 31]. This inspired the exploration of heterojunctions formed by Bi/MoS_2 nanoparticles, anticipating heightened ROS generation and an enhanced photothermal effect for efficient and rapid sterilization under near-infrared light irradiation.

In this study, we developed a nanocomposite gel doped with Bi/MoS_2 heterojunctions for the rapid and effective treatment of diabetic wounds. The synthesis involved the hydrothermal growth of MoS_2 nanomaterials, followed by the deposition of Bi elemental materials onto MoS_2 surfaces through a liquid-phase reaction, resulting in Bi/MoS_2 heterojunctions. Subsequently, Bi/MoS_2-incorporated fibrinogen and thrombin were spray-mixed to produce a Bi/MoS_2-incorporated fibrin gel. The resulting Bi/MoS2-incorporated fibrin gel, chosen for its release of cell growth factors and promotion of endothelial cell migration[32], demonstrated outstanding photocatalytic performance and enhanced heat generation under 808 nm near-infrared light irradiation. The synergistic effect of PCA and PTA exhibited remarkable antibacterial efficacy, promoting efficient wound healing in diabetic mice with *Staphylococcus aureus* infection (Scheme 1). Crucially, the composite gel achieved a 99.7% bacterial eradication rate under 10-minute 808 nm near-infrared light irradiation, highlighting its potential for rapid and efficient sterilization. This work represented a significant advancement in the antibacterial development of metal sulfides, offering a promising strategy for diabetic wound healing.

2. Materials and methods

2.1 Materials

Bismuth nitrate pentahydrate ($Bi(NO_3)_3 \cdot 5H_2O$, AR, 99%), calcium chloride ($CaCl_2$, AR), thiourea (TU, CH_4N_2S, AR, 98%), and sodium borohydride ($NaBH_4$, AR, 98%) were obtained from Aladdin Biochemical Technology Co., Ltd. (Shanghai, China). Polyethylene glycol (PEG, MW=20000) was sourced from Sinopharm Chemical Reagent Co., LTD (Shanghai, China). Ammonium molybdate tetrahydrate

($H_{24}Mo_7N_6O_{24}·4H_2O$, AR, 99%) was acquired from Tianjin Damao Chemical Reagent Factory (Tianjin, China). Bovine fibrinogen (MW: 340 kDa) and lyophilized thrombin powder were purchased from Yeasen Biotech (Shanghai, China) and Hunan Yige Pharmaceutical Co., Ltd. (Xiangtan, China), respectively.

2.2 Synthesis of MoS_2 nanoflowers and Bi/MoS_2-FG

In the synthesis process, MoS_2 nanoflowers were initially prepared via a hydrothermal route. Here, 0.50 g of polyethylene glycol (PEG) was dissolved in 20 mL of deionized water, followed by dissolving 0.1766 g of $H_{24}Mo_7N_6O_{24}·4H_2O$ in the solution. Subsequently, 10 mL of a 2 mmol thiourea (TU) water solution was added and stirred until a transparent solution was obtained. This mixture was then transferred into a 100 mL Teflon-lined autoclave, heated to 180°C, and maintained for 12 h. After natural cooling, the black MoS_2 nanoflowers product was collected, washed with ethanol and deionized water thrice, and finally vacuum-dried to obtain MoS_2 powder for subsequent experiments.

Following the MoS_2 nanoflowers synthesis, 150 mg of MoS_2 was dispersed in 25 mL deionized water, and 2 mmol $Bi(NO_3)_3·5H_2O$ was added to the solution with 15 minutes of magnetic stirring. A certain concentration of $NaBH_4$ (15 mL, 75 mmol/L) was swiftly added to the mixed solution, followed by 10 minutes of magnetic stirring. After the reaction, the products were collected by centrifugation, washed, and finally dried under vacuum to obtain Bi/MoS_2 nano-heterojunction.

Subsequently, fibrin gels (FG) were synthesized by spraying equal volumes of thrombin (10 mg/mL) and fibrinogen (50 U/mL) with or without Bi/MoS_2. The resulting hydrogels, with Bi/MoS_2 heterojunction power concentrations of 0, 0.001, 0.005, and 0.010 g/mL, were denoted as Fibrin Gel, Bi/MoS_2-FG1 (BMFG-1), Bi/MoS_2-FG5 (BMFG-5), and Bi/MoS_2-FG5 (BMFG-10), respectively.

2.3 Characterization

Morphological and microstructural analyses were conducted using field-emission scanning electron microscopy (FE-SEM, Carl Zeiss, Germany) coupled with energy-dispersive X-ray spectroscopy (EDS) and transmission electron microscopy (TEM, Talos F200x, Thermo Fisher, USA). The structural and elemental composition of Bi/MoS_2 was characterized by X-ray diffraction (XRD, Empyrean, Panaco Netherlands) and X-ray photoelectron spectroscopy (XPS, ESCALABXI, Americ). The projector augmented plane-wave method is used to calculate the correlation results with the support of density functional theory. UV-Vis-NIR absorption spectra were obtained using ultraviolet-visible diffuse reflection (UV-Vis-NIR DRS, SHIMADZU UV-3600 Plus) with a self-supporting sample cell, using pure $BaSO_4$ as a reflectance standard. Photoluminescence spectra (PL) were acquired on the FLS980 (Edinburgh, England). Rheological analysis of the gels was performed on a rotating rheometer (MCR301, Austria). The gel storage modulus (G') and loss modulus (G'') were measured as the frequency increased from 0.1 rad/s to 10 rad/s. The hydrogels were thoroughly immersed in PBS overnight. After weighing the full swollen quality(W_s), and the dry quality(W_d) was obtained by drying totally swollen hydrogels to constant weight at around 60°C temperature in vacuum, the formula$(W_s-W_d)/W_d$ was used to calculate the swelling ratio. The photocurrent of the materials was tested through an electrochemical workstation (ZAHNER, Germany) under conditions where the 808 nm near-infrared light source (1.5 $W \cdot cm^{-2}$) was switched on and off for 60 s in Na_2SO_4 solution (0.5 M).

The photothermal experiment of nanomaterials involved ultrasonically dispersing nano-flower samples with phosphate buffer (PBS) and adding them to 48-well plates, with pure PBS solution as the control. The samples were irradiated with 808 nm near-infrared light for 5 minutes, and the real-time temperature of the solution was recorded by an infrared imager. For the gel samples, the gel was prepared in the 48-well plate, and PBS was added to examine the gel sample temperature under 10 minutes of light.

Reactive oxygen species detection kit (100 tests, Jiangsu KGI Biologics) and multifunctional enzyme marker (Switzerland Tecan) were employed to test the

materials' ability to produce reactive oxygen species (ROS). ROS produced by the materials under 808 nm near-infrared light oxidize non-fluorescent DCFH into DCF with strong green fluorescence. The fluorescence intensity of DCF was detected by the microplate reader to explore the level of ROS produced by the materials.

2.4 Antibacterial activity in vitro

Staphylococcus aureus (*S. aureus*) and *Escherichia coli* (*E. coli*) were used to assess the antibacterial properties of the materials *in vitro*. The *in vitro* antibacterial activity was studied using the plate colony counting method. The nanomaterials were prepared into the bacterial suspension containing 500 μg/mL of material (10^6 CFU/mL), or 10^6 CFU/mL suspension was added to the gel samples. After dark treatment or irradiation for 5 minutes, the suspension was diluted to an appropriate concentration, and 50 μL of the diluted bacterial solution was spread onto a culture plate covered with solid agar and incubated at 37°C. The agar plates were photographed and counted after the bacteria colonies grew. The antibacterial rate was calculated using the formula: Antibacterial efficiency (%) = $(1 - N/N_0) \times 100$, where N and N_0 represent the number of bacteria colonies in the experimental and control groups, respectively.

In addition, the antibacterial activity of the materials was evaluated using the LIVE/DEAD®BacLight™ bacterial activity kit. The PI dye cannot penetrate the complete bacterial membrane, but it can penetrate the damaged bacteria and fluoresce red when it binds to the nucleic acid inside. At the same time, the SYTO®9 dye binds to the membrane of living bacteria and emits green fluorescence. The fluorescence color can estimate whether the bacteria are alive or dead. The dark or light treated bacterial suspension and blended dye solution were added to the pore plate, incubated for 20 minutes away from light. Subsequently, The fluorescence staining was observed by inverted fluorescence microscope (Zeiss).

2.5 Cell experiments

The biotoxicity of the hybrid gels was measured by CCK-8 kit and live/dead staining. In short, HUVECs cells (5×10^4 cells/well) were inoculated on the gel sample in a 48-

well plate and cultured at 5% CO_2 and 37℃ for 1 and 5 days. The cell viability of the cells was evaluated by CCK-8 method. Live/dead staining was performed using the dye Calcein-AM and PI. The cells (48-well plate, 1×10^4 cells/well), stained with Calcein-AM /PI live/dead dye after cultured for 1 day, and observed to distinguish the live and dead cells through inverted fluorescence microscope.

2.6 Animal Experiments

All experimental procedures at the animal level were performed under the approval of the Animal Care Committee of South China University of Technology (approval number: 2022100). The male BALB/C mice (6-7 weeks old) used in this experiment were purchased from Jingxi Nanfang Hospital. The animals were fed in accordance with the Animal Management Rules of the Ministry of Health of the People's Republic of China and the Guidelines for the Care and Use of Laboratory Animals of China. Mice were injected with 50 mg/kg streptozotocin solution for 5 days consecutively, and mice with blood glucose level above 16.7 mM were selected as experimental objects. Two wounds with a diameter of 7 mm were cut on the back of each mouse with a hole punch, and 50 μL bacterial suspension (10^8 CFU/mL) was added to the wound to establish a infection model of diabetic skin wound. The model was divided into four groups randomly (each group containing three mice): control group, fibrin gel group, BMFG group and BMFG+808 group. The wounds were cleaned with normal saline and treated accordingly. Concretely, the control group was treated with normal saline only, the fibrin gel group and the BMFG group were handled with fibrin gel and Bi/MoS_2 composite gel respectively, and the BMFG+808 group was treated with Bi/MoS_2 composite gel and irradiated 808 nm NIR for 10 minutes. Subsequently, the gels were changed every 2 days, and the wounds healing were photographed at 0, 2, 4, 8 and 14 days. Beyond that, mice were randomly selected and killed at 4, 8 and 14 days respectively, and the skin at the wound site was collected for histology and immunofluorescence staining. Specifically, Hematoxylin and eosin (H&E) and Masson staining were used to observe the histomorphological changes of soft tissue, Giemsa staining was used to evaluate the residual bacteria at the wound, and CD31 staining was

used to detect the angiogenesis.

2.7 Statistical Analysis

Results were expressed as mean ± SD (standard deviation). All data were acquired from three to five independent experiments. Origin 2018 and GraphPad Prism 8 were performed for all statistical analyses, and images were analyzed by ImageJ.

3. Results and discussion

3.1 Formation and characterization of Bi/MoS_2 heterojunction-loaded fibrin gel

The MoS_2 nanoflowers was successfully synthesized using the hydrothermal method as previously reported[33]. Subsequently, the Bi/MoS_2 composite was synthesized through an in-situ reduction process. SEM images in Fig. 1a, b revealed the flowerlike structures of MoS_2, with Bi nanoparticles intricately grown on the surface of MoS_2 nanospheres. The calculated average sizes of the MoS_2 nanoflowers are approximately 300-400 nm. EDS element mapping (Fig. S1) illustrated the uniform distribution of related elements on both MoS_2 and Bi/MoS_2. Further confirmation of the composition was provided by Fig. 1c, showing that MoS_2 nanoflowers are composed of multilayered nanosheets arranged randomly. In the fringe patterns of Fig. 1d, the d-spacings of Bi/MoS_2 were identified as 0.64 nm and 0.33 nm, corresponding to the (100) plane of MoS_2 and the (012) plane of the Bi nanoparticles, respectively[34-36].

Fig. 1e presented XRD patterns of MoS_2 and Bi/MoS_2, with MoS_2 peaks aligning with the standard map (PDF#37-1492) and the appearance of a distinct diffraction peak at 27.2° in the reduced powder Bi/MoS_2 XRD pattern, confirming the successful reduction and coverage of Bi on MoS_2[37]. The chemical state of the nanomaterials was assessed using XPS (Fig. 1f). MoS_2 exhibited the presence of O, N, C, Mo, and S elements, while Bi/MoS_2 showed additional peaks corresponding to Bi. High-resolution spectra (Fig. 1g, h) confirmed successful adhesion of Bi nanoparticles to MoS_2. The binding energies of Mo 3d5/2, Mo 3d3/2, and Mo^{6+} peaks were located at 228.2 (±0.1) eV, 231.7 (±0.2) eV, and 235.2 eV, respectively, and a characteristic peak of 225.4 (±

0.1) eV in the Mo 3d spectrum indicated S 2s[27, 34, 35, 38]. The high-resolution map of the Bi element (Fig. 1h) showed Bi exclusively in Bi/MoS_2, not in MoS_2, with peaks for Bi 4d5/2 and Bi 4d3/2 observed at 442.12 eV and 465.8 eV, respectively[39]. This comprehensive characterization solidifies the successful preparation of the Bi/MoS_2 heterojunction nanocomplex.

COMSOL finite element analysis simulation (Fig. 2a) showed that the electromagnetic field on the top of Bi nanoparticles was significantly enhanced under 808nm near-infrared light. This phenomenon proved that LSPR effect exists in Bi/MoS_2 heterojunction, which can accelerate carrier migration. To further understand the electronic interactions, we conducted density functional theory calculations (Fig. 2b-d)[40, 41]. The results illustrated that Bi atoms lose electrons while MoS_2 gains electrons at the interface, signifying electron transfer from Bi to MoS_2. The band structure diagram in Fig. 2e indicated metallic characteristics for Bi/MoS_2, facilitating charge separation and transfer under external forces. The density of states calculations (Fig. 2f) revealed that the electronic states near the Fermi level are mainly occupied by Bi-p orbitals, confirming the metallic properties of Bi/MoS_2 and further supporting its efficacy in charge separation and transfer.

The optical characteristics of both MoS_2 and the Bi/MoS_2 nanocomposite were thoroughly investigated through a suite of methods, providing valuable insights into their photoelectric performance. The UV-vis-NIR absorption spectra (Fig. 3a) revealed the extensive optical absorption capabilities of MoS_2 and Bi/MoS_2 across the visible to NIR region. Additionally, the Bi/MoS_2 spectra exhibited a distinct semiconductor absorption edge at 300 nm. For a more nuanced understanding of electron and hole separation efficiency, the PL spectrum (Fig. 3b) was employed. MoS_2 exhibited a higher PL emission peak intensity compared to Bi/MoS_2, indicating that the introduction of Bi nanoparticles effectively mitigated the recombination of photogenerated electrons and holes. This enhancement underscored the superior photodynamic performance of Bi/MoS_2. The photocurrent property was evaluated during the 808 nm NIR photo on/off cycle, and the results (Fig. 3c) clearly demonstrated a stronger photocurrent response

for Bi/MoS_2 compared to MoS_2. This heightened response was primarily attributed to the superior transport efficiency of Bi/MoS_2 over MoS_2. These findings unequivocally validate that the composited Bi/MoS_2 exhibits optimized photoelectric performance. The superior separation and migration of photogenerated carriers in Bi/MoS_2 suggested its promising potential in diverse applications. Particularly, the enhanced photodynamic performance positions Bi/MoS_2 as a compelling candidate for applications requiring efficient photoresponsive behavior.

Meanwhile, the photothermal absorbance behavior of the nanomaterials was meticulously investigated under irradiation with an 808 nm laser (Fig. S2a). Following a 5-minute irradiation period, the PBS control group experienced a mere 2.5℃ temperature increase, contrasting with MoS_2 and Bi/MoS_2 nanomaterials, which exhibited about 30℃ increase from the initial room temperature of approximately 25℃. This observation underscores the superior photothermal properties of both MoS_2 and Bi/MoS_2. Additionally, the nanomaterials' capacity to generate reactive oxygen species (ROS) was assessed (Fig. S2b). Remarkably, the control group exhibited negligible ROS production within the 5-minute timeframe. In contrast, both MoS_2 and Bi/MoS_2 demonstrated a notable ability to generate ROS under the same conditions, with Bi/MoS_2 exhibiting a particularly impressive tenfold increase compared to its counterpart. This discrepancy can be attributed to the Bi/MoS_2 heterojunction's facilitation of the separation of photogenerated carriers under 808 nm NIR laser irradiation. The isolated carriers undergo oxidation or reduction reactions, resulting in the production of a substantial quantity of ROS. This ROS generation serves as a foundational mechanism contributing to the materials' exceptional antibacterial properties.

Finally, the Bi/MoS_2 heterojunction was integrated into the fiber gel. Fig. 4a-d depicted the SEM images of the surface and cross-section of the Bi/MoS_2 composite fiber gel. Remarkably, the gel exhibited a porous network structure irrespective of the inclusion of Bi/MoS_2 nanomaterials, with tightly cross-linked fibers. Furthermore, the nanomaterials were uniformly embedded within the composite gel, and as the doping

amount increased, the nanomaterials exhibited a proportional augmentation in the gel network structure, accentuating agglomeration tendencies. Elemental analysis results (Fig. S3) underscored a significant enhancement in the signal of the typical element Bi with an increase in doping density.

Rheological test results, depicted in Fig. 4e, revealed that the loss modulus (G'') for all samples remain lower than the storage modulus (G') across the angular frequency range from 0.1 to 10 rad/s, indicative of a relatively stable network structure for all gels. As shown in Fig. S4, the swelling ratios of the Fibrin Gel, BMFG-1, BMFG-5, and BMFG-10 samples were 70.83 ± 3.93, 69.86 ± 2.16, 72.64 ± 6.09, and 70.82 ± 5.12, respectively. These values suggest that the gels have consistent swelling behaviors, which is important for their application in wound healing.

Moreover, Fig. 4f illustrated the heating curves of gels under laser exposure for 10 minutes. In the control group (Fibrin Gel), the temperature increased modestly by 2.9℃ (from 29.3℃ to 32.2℃). Contrastingly, one of the experimental group, BMFG-1, exhibited minimal temperature change (increased by 7.3℃). However, the BMFG-5 and BMFG-10 groups demonstrated pronounced photothermal properties, with temperatures rising by 23.8℃ (from 29.1 to 52.9) and 33.6℃ (from 28.5 to 62.1), respectively, after 10 minutes of laser illumination. In summary, the photothermal properties of the gel samples exhibited a positive correlation with the doping concentration of Bi/MoS_2. Furthermore, the results of ROS generation by the gels were presented in Fig. 4g. The data indicated that the gels' ability to generate ROS under light increased with rising doping content. Specifically, the BMFG-5 and BMFG-10 groups produced approximately 9 and 14 times more ROS than the original concentration after 10 minutes of 808 nm NIR laser irradiation. The observed trends highlighted the tunability of these properties by adjusting the doping concentration, showcasing the versatility and potential of Bi/MoS_2-incorporated fibrin gel for wound healing.

3.2 Antibacterial properties, cytotoxicity assay, cell migration and tube formation in

vitro of Bi/MoS_2 heterojunction-loaded fibrin gel

The antibacterial activities of nanomaterials and complex hydrogels against *S. aureus* and *E. coli* were assessed, with a specific focus on *S. aureus*, a prevalent bacterium in diabetic wound infections. The relevant results for nanomaterials were illustrated in Fig. S5. Fig. S5a, b presented plate colony count images and antibacterial ratios for *S. aureus*, while Fig. S5c, d depicted the corresponding results for *E. coli.* In the absence of light exposure, bacterial colonies in all groups exhibited robust growth, with no discernible antibacterial activity. However, under 808 nm NIR laser irradiation for 5 minutes at a power of 1.5 $W \cdot cm^{-2}$, the experimental groups demonstrated significant antibacterial activities, surpassing the efficacy of the control group. Notably, the Bi/MoS_2 group exhibited antibacterial rates of 99.2% against *S. aureus* and 99.7% against *E. coli*, outperforming the MoS_2 group. This heightened antibacterial effect was attributed to the combined action of Bi/MoS_2 photothermal and ROS effects on bacteria under light, aligning with the observed photothermal properties and ROS generation capabilities of the material.

The antibacterial properties of Bi/MoS_2 composite gels against *S. aureus* were further evaluated using live/dead staining and plate coating. Fig. 5a-c showcased fluorescence images, plate colony count results, and quantification outcomes for *S. aureus*, respectively. In the control group (Fibrin Gel), abundant green fluorescence indicated intact bacterial membranes (Fig. 5a). Conversely, composite gels doped with Bi/MoS_2 heterojunction emitted red fluorescence post-illumination, signifying bacterial membrane damage. Notably, BMFG-5 and BMFG-10 groups exhibited nearly complete bacterial membrane damage, emitting intense red fluorescence. Unlike Fibrin Gel, which displayed minimal antibacterial effect under light, composite gels demonstrated pronounced antibacterial properties under equivalent conditions (Fig. 5b, c). Moreover, with increasing heterojunction doping concentration, the anti-*S. aureus* activity of the gels significantly intensified, with BMFG-5 and BMFG-10 demonstrating excellent antibacterial properties. Specifically, the antibacterial rates against *S. aureus* were 97.5%

for BMFG-5 and 99.7% for BMFG-10. Thus, appropriately Bi/MoS_2-doped compound gels exhibited a bactericidal effect on wound bacteria in diabetic conditions under 808 nm NIR irradiation. Furthermore, Fig. S6 depicted the bactericidal effect of complex gels on *E. coli*, with results broadly consistent with those for *S. aureus*. The exceptional antibacterial properties of the gels underscored their potential role in the diabetic wound healing process. These findings highlighted the promise of Bi/MoS_2 composite gels as a therapeutic intervention for effectively combating bacterial infections in diabetic wounds.

The cytotoxicity assessment of both nanomaterials and hybrid gels was conducted through live/dead fluorescence staining and CCK-8 assays. The correlational results between cells and nanomaterials after 24 hours of culture were presented in Fig. S7. The results demonstrated that both MoS_2 and Bi/MoS_2 exhibited no significant differences compared to the control group, indicating the absence of apparent cytotoxicity for these nanomaterials. Moving forward, the evaluation of gels cytotoxicity was depicted in Fig. 5d, e. In the live/dead staining images (Fig. 5d), no noticeable distinctions were observed between the control group and the gel samples, with nearly all cells emitting green fluorescence rather than red fluorescence. The proliferation data for the gel samples after 1 and 5 days of culture (Fig. 5e) illustrated robust cell activity in all groups, suggesting the ability of the composite gel samples to promote cell proliferation. These findings collectively affirmed the non-cytotoxic nature and commendable biocompatibility of the composite gel samples. The cytotoxicity of the Bi/MoS_2-incorporated fibrin gel with irradiation was assessed using the CCK-8 assay. As shown in Fig. S8, cells treated with the Bi/MoS_2-incorporated fibrin gel and subjected to 808 nm NIR irradiation for 10 minutes exhibited a reduction in viability compared to the non-irradiated groups. And the viability of BMFG-5 gel remained above 85%. However, Cells treated with the BMFG-10-incorporated fibrin gel and subjected to 808 nm NIR irradiation for 10 minutes exhibited a noticeable reduction in viability compared to the non-irradiated groups. These results demonstrated that while the BMFG-10-incorporated fibrin gel maintains good

biocompatibility without NIR irradiation, its enhanced photothermal and photocatalytic properties under NIR irradiation lead to increased cytotoxicity. The BMFG-5 gel, which exhibited lower cytotoxicity under similar conditions, may therefore be more suitable for applications where cell viability is critical.

To evaluate the role of the sprayed composite gel in promoting angiogenesis, an *in vitro* angiogenesis assay was performed. After culturing for 24 h HUVECs, the cells were photographed in a bright field (Fig. S9a). The capillary tube branches number was analyzed with ImageJ software to quantify the angiogenesis process (Fig. S9c). Figure R1a and R1c demonstrated that the fibrin gel could promoted formation of tubular structures *in vitro*. To further elucidate the effect of the composite gel on cell migration, we employed a scratch assay. HUVEC cell were incubated on the surface of composite gel. And then a controlled scratch was created. After a 24-hour incubation period, remarkable cell migration and wound closure were observed in the composite gel group (Fig. S9b, d). The wound area in the test group exhibited a substantial reduction to 49.25% compared to the initial wound size. In contrast, the negative control group displayed a less pronounced wound closure, with 79.42% of the wound area remaining (Fig. S9d). These findings suggested that the composite gel has the potential to promote wound healing and skin regeneration.

3.3 Bi/MoS_2 heterojunction-loaded fibrin gel enhanced wound healing, fostered angiogenesis, eliminated bacteria, and mitigated inflammation in diabetic mice

To assess the reparative effects of compound gels on diabetic wounds, an *in vivo* animal model of diabetic wound infection was established. The BMFG-5 group, selected based on its optimal antibacterial efficacy and biocompatibility, was subjected to experimentation. The experimental process was shown in the Fig. 6a. Two wounds were created on each mouse, categorized into four groups: Control group, Fibrin Gel group, BMFG group, and BMFG+NIR group (808 nm NIR irradiation for 10 minutes per 2-day). The progression of wound healing was documented through photographs at 0, 2, 4, 8, and 14 days after the respective treatments, as illustrated in Fig. 6b. After 2 days, bacterial infection with ichor was evident in all groups. However, the

BMFG+NIR group exhibited less severe infection compared to other groups, showcasing its superior performance. Notably, after 4 days of treatment, distinctions in wound healing between the BMFG+NIR group and the other groups became apparent. Moreover, at the two-week mark, the BMFG+NIR group displayed a reduced trauma area and more advanced healing compared to the other three groups. This observation indicated that 808 nm NIR played a pivotal role in the BMFG-mediated promotion of diabetic wound healing. The enhanced wound healing in the BMFG+NIR group can be attributed to the combined effects of light-induced heat and ROS production by the gel compounded with Bi/MoS_2 under NIR irradiation. This dual-action mechanism contributed to the elimination of bacteria around the wound, thereby facilitating the wound repair process. The results underscored the therapeutic potential of the BMFG gel in the context of diabetic wound management under illumination.

The assessment of diabetic wound healing at different phases was conducted through histological section staining, employing Hematoxylin and eosin (H&E) and Masson staining for a comprehensive analysis of re-epithelialization, connective tissue formation, and collagen production, as presented in Fig. 7a-c. In the H&E staining images (Fig. 7a), noticeable subcutaneous congestion and inflammatory cell infiltration were observed across all groups after 4 days. Particularly, the Control, Fibrin Gel, and BMFG groups exhibited varying degrees of inflammation. Upon examination of the staining images 14 days later, a discernible degree of re-epithelialization and connective tissue formation were evident in all groups, with the BMFG+NIR group showcasing more pronounced results. Intriguingly, the appearance of skin hair follicles in the BMFG+NIR group indicated a relatively intact skin structure. Masson staining (Fig. 7b) showcased loose and disordered collagen fibers in all groups after 4 days. However, the arrangement of collagen fibers notably improved after 14 days, with the BMFG+NIR group demonstrating more distinct and close arranged morphology compared to the other three groups. Assessment of angiogenic properties using CD31 staining (Fig. 7c) revealed more pronounced and clearer neovascularization in the wounds of the BMFG+NIR group, highlighted by red arrow points in the images. This indicated

enhanced angiogenesis in response to NIR irradiation.

Furthermore, Giemsa staining images (Fig. 7d) were utilized to detect bacterial residues at the wound sites. On the 4th day, numerous bacteria were observed in all three groups, except for the BMFG+NIR group. This compellingly suggested the effective antibacterial action of the BMFG+NIR group against *S. aureus* in diabetic wounds. And Bacteria were extracted from the wound tissue and cultured on agar medium for colony counting. The results were then compared with those found in the skin at the wound site (Fig. S10). The collective findings underscored the remarkable efficacy of the BMFG-5 composite fibrin gel in swiftly and effectively eliminating bacterial infection in infected wounds under NIR irradiation. Additionally, the gel promoted re-epithelialization, connective tissue and hair follicle formation, orderly arrangement of collagen fibers, and new angiogenesis, collectively fostering an environment conducive to accelerated wound healing. In general, the BMFG+NIR group exhibited outstanding effects in promoting diabetic wound healing.

In this study, we developed a nanocomposite gel doped with Bi/MoS2 heterojunctions for the rapid and effective treatment of diabetic wounds. Compared to the reported injectable hydrogel dressings [42-43], our Bi/MoS_2-incorporated fibrin gel offers several distinct advantages: The gel's ability to release cell growth factors and promote endothelial cell migration further enhances its wound healing capabilities. The spray-mixed formulation of our hydrogel facilitates easy and practical application in clinical settings, which is advantageous over some injectable formulations that may require more precise administration techniques. Future research should focus on investigating the long-term effects of NIR irradiation and ROS generation on tissues to ensure safety [44]. Additionally, developing hydrogel formulations that can be tailored for specific medical conditions will expand their application scope.

4. Conclusion

In summary, we successfully engineered a Bi/MoS_2 heterojunction complex fibrin gel exhibiting dual functionalities of photodynamic therapy (PDT) and photothermal

therapy (PTT), effectively eradicating *S. aureus* through the synergistic action of photothermal effects and ROS generation under 808 nm NIR light irradiation. Notably, the hydrogel displayed remarkable antibacterial properties with only 10 minutes of irradiation, underscoring its rapid and efficient bactericidal capabilities. This accelerated antibacterial efficacy is primarily attributed to the concerted disruption of bacterial membranes by photothermal effects and ROS, and the damaged bacterial membrane further facilitates the entry of ROS into bacteria and expediting protein oxidation. Simultaneously, photothermal effects accelerate protein inactivation, culminating in the demise of bacteria in both *in vivo* and *in vitro* settings. Animal experiments further validated the exceptional bactericidal efficacy of the compound gel under light exposure, concurrently promoting re-epithelialization, collagen hyperplasia, and the formation of new blood vessels to facilitate the repair of diabetic wounds. This study introduced a straightforward and highly efficient approach for treating diabetic wounds, showcasing significant potential in addressing skin infections and offering a novel avenue for drug-resistant antimicrobial therapy.

Acknowledgments

This work was financially supported by the National Key Research and Development Program of China (2022YFC2406000, 2021YFC2400402), the National Natural Science Foundation of China (52101285, 51932002, U21A2055, U22A20160), the Guangzhou Applied Basic Research Project (202201010597).

References

[1] Y. Qian, Y. Zheng, J. Jin, X. Wu, K. Xu, M. Dai, Q. Niu, H. Zheng, X. He, J. Shen, Immunoregulation in diabetic wound repair with a photoenhanced glycyrrhizic acid hydrogel scaffold, Adv. Mater. 34 (2022) 2200521. https://doi.org/10.1002/adma.202200521.

[2] J. Yang, W. Zeng, P. Xu, X. Fu, X. Yu, L. Chen, F. Leng, C. Yu, Z. Yang, Glucose-responsive

multifunctional metal-organic drug-loaded hydrogel for diabetic wound healing, Acta Biomater. 140 (2022) 206-218. https://doi.org/10.1016/j.actbio.2021.11.043.

[3] T. Ma, X. Zhai, Y. Huang, M. Zhang, X. Zhao, Y. Du, C. Yan, A smart nanoplatform with photothermal antibacterial capability and antioxidant activity for chronic wound healing, Adv. Healthcare Mater. 10 (2021) e2100033. https://doi.org/10.1002/adhm.202100033.

[4] Y. Wang, Q. Lv, Y. Chen, L. Xu, M. Feng, Z. Xiong, J. Li, J. Ren, J. Liu, B. Liu, Bilayer hydrogel dressing with lysozyme-enhanced photothermal therapy for biofilm eradication and accelerated chronic wound repair, Acta Pharm. Sin. B 13 (2023) 284-297. https://doi.org/10.1016/j.apsb.2022.03.024.

[5] Z. Wang, X. Liu, Y. Duan, Y. Huang, Infection microenvironment-related antibacterial nanotherapeutic strategies, Biomaterials 280 (2022) 121249. https://doi.org/10.1016/j.biomaterials.2021.121249.

[6] T.R. McCulloch, T.J. Wells, F. Souza-Fonseca-Guimaraes, Towards efficient immunotherapy for bacterial infection, Trends Microbiol. 30 (2022) 158-169. https://doi.org/10.1016/j.tim.2021.05.005.

[7] J. Han, S. Zeng, Y. Chen, H. Li, J. Yoon, Prospects of coupled iron-based nanostructures in preclinical antibacterial therapy, Adv. Drug Deliver. Rev. 193 (2023) 114672. https://doi.org/10.1016/j.addr.2022.114672.

[8] J. Xuan, W. Feng, J. Wang, R. Wang, B. Zhang, L. Bo, Z.S. Chen, H. Yang, L. Sun, Antimicrobial peptides for combating drug-resistant bacterial infections, Drug Resist. Updat. 68 (2023) 100954. https://doi.org/10.1016/j.drup.2023.100954.

[9] J. Li, F. Lv, J. Li, Y. Li, J. Gao, J. Luo, F. Xue, Q. Ke, H. Xu, Cobalt-based metal-organic

framework as a dual cooperative controllable release system for accelerating diabetic wound healing, Nano Res. 13 (2020) 2268-2279. https://doi.org/10.1007/s12274-020-2846-1.

[10] P. Makvandi, C.Y. Wang, E.N. Zare, A. Borzacchiello, L.N. Niu, F.R. Tay, Metal-based nanomaterials in biomedical applications: Antimicrobial activity and cytotoxicity aspects, Adv. Funct. Mater. 30 (2020) 1910021. https://doi.org/10.1002/adfm.201910021.

[11] Q. Xin, H. Shah, A. Nawaz, W. Xie, M.Z. Akram, A. Batool, L. Tian, S.U. Jan, R. Boddula, B. Guo, Q. Liu, J.R. Gong, Antibacterial carbon-based nanomaterials, Adv. Mater. 31 (2019) e1804838. https://doi.org/10.1002/adma.201804838.

[12] A. Maleki, J. He, S. Bochani, V. Nosrati, M.A. Shahbazi, B. Guo, Multifunctional photoactive hydrogels for wound healing acceleration, ACS Nano 15 (2021) 18895-18930. https://doi.org/10.1021/acsnano.1c08334.

[13] X. Qi, Y. Huang, S. You, Y. Xiang, E. Cai, R. Mao, W. Pan, X. Tong, W. Dong, F. Ye, J. Shen, Engineering robust Ag-decorated polydopamine nano-photothermal platforms to combat bacterial infection and prompt wound healing, Adv. Sci. 9 (2022) 2106015. https://doi.org/10.1002/advs.202106015.

[14] M. Godoy-Gallardo, U. Eckhard, L.M. Delgado, Y.J.D. de Roo Puente, M. Hoyos-Nogués, F.J. Gil, R.A. Perez, Antibacterial approaches in tissue engineering using metal ions and nanoparticles: From mechanisms to applications, Bioact. Mater. 6 (2021) 4470-4490. https://doi.org/10.1016/j.bioactmat.2021.04.033.

[15] H.H. Lara, E.N. Garza-Trevino, L. Ixtepan-Turrent, D.K. Singh, Silver nanoparticles are broad-spectrum bactericidal and virucidal compounds, J. Nanobiotechnol. 9 (2011) 30. https://doi.org/10.1186/1477-3155-9-30.

[16] X.Y. Kong, X.M. Liu, Y.F. Zheng, P.K. Chu, Y. Zhang, S.L. Wu, Graphitic carbon nitride-based materials for photocatalytic antibacterial application, Mat. Sci. Eng. R. 145 (2021) 100610. https://doi.org/10.1016/j.mser.2021.100610.

[17] Y. Wang, Y. Jin, W. Chen, J. Wang, H. Chen, L. Sun, X. Li, J. Ji, Q. Yu, L. Shen, B. Wang, Construction of nanomaterials with targeting phototherapy properties to inhibit resistant bacteria and biofilm infections, Chem. Eng. J. 358 (2019) 74-90. https://doi.org/10.1016/j.cej.2018.10.002.

[18] R. Dong, B. Guo, Smart wound dressings for wound healing, Nano Today 41 (2021) 101290. https://doi.org/10.1016/j.nantod.2021.101290.

[19] T. Wei, Q. Yu, H. Chen, Responsive and synergistic antibacterial coatings: Fighting against bacteria in a smart and effective way, Adv. Healthcare Mater. 8 (2019) e1801381. https://doi.org/10.1002/adhm.201801381.

[20] J. Huo, Q. Jia, H. Huang, J. Zhang, P. Li, X. Dong, W. Huang, Emerging photothermal-derived multimodal synergistic therapy in combating bacterial infections, Chem. Soc. Rev. 50 (2021) 8762-8789. https://doi.org/10.1039/d1cs00074h.

[21] Y. Liang, J. He, B. Guo, Functional hydrogels as wound dressing to enhance wound healing, ACS Nano 15 (2021) 12687-12722. https://doi.org/10.1021/acsnano.1c04206.

[22] H. Zhang, X. Sun, J. Wang, Y. Zhang, M. Dong, T. Bu, L. Li, Y. Liu, L. Wang, Multifunctional injectable hydrogel dressings for effectively accelerating wound healing: Enhancing biomineralization strategy, Adv. Funct. Mater. 31 (2021) 2100093. https://doi.org/10.1002/adfm.202100093.

[23] M. Alizadehgiashi, C.R. Nemr, M. Chekini, D. Pinto Ramos, N. Mittal, S.U. Ahmed, N. Khuu, S.O. Kelley, E. Kumacheva, Multifunctional 3D-printed wound dressings, ACS Nano 15 (2021)

12375-12387. https://doi.org/10.1021/acsnano.1c04499.

[24] X. Qi, Y. Xiang, E. Cai, S. You, T. Gao, Y. Lan, H. Deng, Z. Li, R. Hu, J. Shen, All-in-one: Harnessing multifunctional injectable natural hydrogels for ordered therapy of bacteria-infected diabetic wounds, Chem. Eng. J. 439 (2022) 135691. https://doi.org/10.1016/j.cej.2022.135691.

[25] F. Wei, X. Cui, Z. Wang, C. Dong, J. Li, X. Han, Recoverable peroxidase-like Fe3O4@MoS2-Ag nanozyme with enhanced antibacterial ability, Chem. Eng. J. 408 (2021) 127240. https://doi.org/10.1016/j.cej.2020.127240.

[26] A.S. Sethulekshmi, A. Saritha, K. Joseph, A.S. Aprem, S.B. Sisupal, MoS2 based nanomaterials: Advanced antibacterial agents for future, J. Control. Release 348 (2022) 158-185. https://doi.org/10.1016/j.jconrel.2022.05.047.

[27] C.Y. Tu, J.M. Wu, Localized surface plasmon resonance coupling with piezophototronic effect for enhancing hydrogen evolution reaction with Au@MoS_2 nanoflowers, Nano Energy 87 (2021) 106131. https://doi.org/10.1016/j.nanoen.2021.106131.

[28] G. Wang, G. Zhang, X. Ke, X. Chen, X. Chen, Y. Wang, G. Huang, J. Dong, S. Chu, M. Sui, Direct synthesis of stable 1T-MoS2 doped with Ni single atoms for water splitting in alkaline media, Small 18 (2022) e2107238. https://doi.org/10.1002/smll.202107238.

[29] J. Yang, H. Yao, Y. Guo, B. Yang, J. Shi, Enhancing tumor catalytic therapy by Co-catalysis, Angew. Chem. Int. Ed. 61 (2022) e202200480. https://doi.org/10.1002/anie.202200480.

[30] M. Y. Qi, Z.R. Tang, Y.J. Xu, Near field scattering optical model-based catalyst design for artificial photoredox transformation, ACS Catal. 13 (2023) 3971-3982. https://doi.org/10.1021/acscatal.2c06397.

[31] M. Sayed, J. Yu, G. Liu, M. Jaroniec, Non-noble plasmonic metal-based photocatalysts,

Chem. Rev. 122 (2022) 10484-10537. https://doi.org/10.1021/acs.chemrev.1c00473.

[32] K. Liu, M. Wiendels, H. Yuan, C. Ruan, P.H.J. Kouwer, Cell-matrix reciprocity in 3D culture models with nonlinear elasticity, Bioact. Mater. 9 (2022) 316-331. https://doi.org/10.1016/j.bioactmat.2021.08.002.

[33] W. Yin, J. Yu, F. Lv, L. Yan, L.R. Zheng, Z. Gu, Y. Zhao, Functionalized nano-MoS_2 with peroxidase catalytic and near-infrared photothermal activities for safe and synergetic wound antibacterial applications, ACS Nano 10 (2016) 11000-11011. https://doi.org/10.1021/acsnano.6b05810.

[34] C. Zhang, J. Wang, R. Chi, J. Shi, Y. Yang, X. Zhang, Reduced graphene oxide loaded with MoS2 and Ag3PO4 nanoparticles/PVA interpenetrating hydrogels for improved mechanical and antibacterial properties, Mater. Des. 183 (2019) 108166. https://doi.org/10.1016/j.matdes.2019.108166.

[35] X. Zhang, G. Zhang, H. Zhang, X. Liu, J. Shi, H. Shi, X. Yao, P.K. Chu, X. Zhang, A bifunctional hydrogel incorporated with CuS@MoS2 microspheres for disinfection and improved wound healing, Chem. Eng. J. 382 (2020) 122849. https://doi.org/10.1016/j.cej.2019.122849.

[36] Y. Wu, X. Yue, J. Fan, X. Hao, Q. Xiang, In situ fabrication of plasmonic Bi/CsPbBr3 composite photocatalyst toward enhanced photocatalytic CO2 reduction, Appl. Surf. Sci. 609 (2023) 155391. https://doi.org/10.1016/j.apsusc.2022.155391.

[37] J. Gong, C.S. Lee, Y.Y. Chang, Y.S. Chang, Novel self-assembled bimetallic structure of Bi/Fe0: The oxidative and reductive degradation of hexahydro-1,3,5-trinitro-1,3,5-triazine (RDX), J. Hazard. Mater. 286 (2015) 107-117. https://doi.org/10.1016/j.jhazmat.2014.10.063.

[38] X. Zhang, C. Zhang, Y. Yang, H. zhang, X. Huang, R. Hang, X. Yao, Light-assisted rapid

sterilization by a hydrogel incorporated with Ag3PO4/MoS2 composites for efficient wound disinfection, Chem. Eng. J. 374 (2019) 596-604. https://doi.org/10.1016/j.cej.2019.05.229.

[39] L. Wang, H. Yin, S. Wang, J. Wang, S. Ai, Ni2+-assisted catalytic one-step synthesis of Bi/BiOCl/Bi2O2CO3 heterojunction with enhanced photocatalytic activity under visible light, Appl. Catal. B-Environ. 305 (2022) 121039. https://doi.org/10.1016/j.apcatb.2021.121039.

[40] B.W.J. Chen, L. Xu, M. Mavrikakis, Computational methods in heterogeneous catalysis, Chem. Rev. 121 (2020) 1007-1048. https://doi.org/10.1021/acs.chemrev.0c01060.

[41] J. Westermayr, P. Marquetand, Machine learning for electronically excited states of molecules, Chem. Rev. 121 (2020) 9873-9926. https://doi.org/10.1021/acs.chemrev.0c00749.

[42] Y. Xiang, X. Qi, E. Cai, C. Zhang, J. Wang, Y. Lan, H. Deng, J. Shen, R. Hu, Highly efficient bacteria-infected diabetic wound healing employing a melanin-reinforced biopolymer hydrogel, Chem. Eng. J., 460 (2023) 141852. https://doi.org/10.1016/j.cej.2023.141852

[43] Y. Xiang, P. Zhuge, X. Qi, X. Ge, J. Xiang, H. Xu, E. Cai, Y. Lan, X. Chen, Y. Li, Y. Shi, J. Shen, J. Liu, A cuttlefish ink nanoparticle-reinforced biopolymer hydrogel with robust adhesive and immunomodulatory features for treating oral ulcers in diabetes, Bioact. Mater., 39 (2024) 562-581. https://doi.org/10.1016/j.bioactmat.2024.04.022

[44] X. Qi, Y. Xiang, E. Cai, X. Ge, X. Chen, W. Zhang, Z. Li, J. Shen, Inorganic–organic hybrid nanomaterials for photothermal antibacterial therapy, Coord. Chem. Rev., 496 (2023) 215426. https://doi.org/10.1016/j.ccr.2023.215426

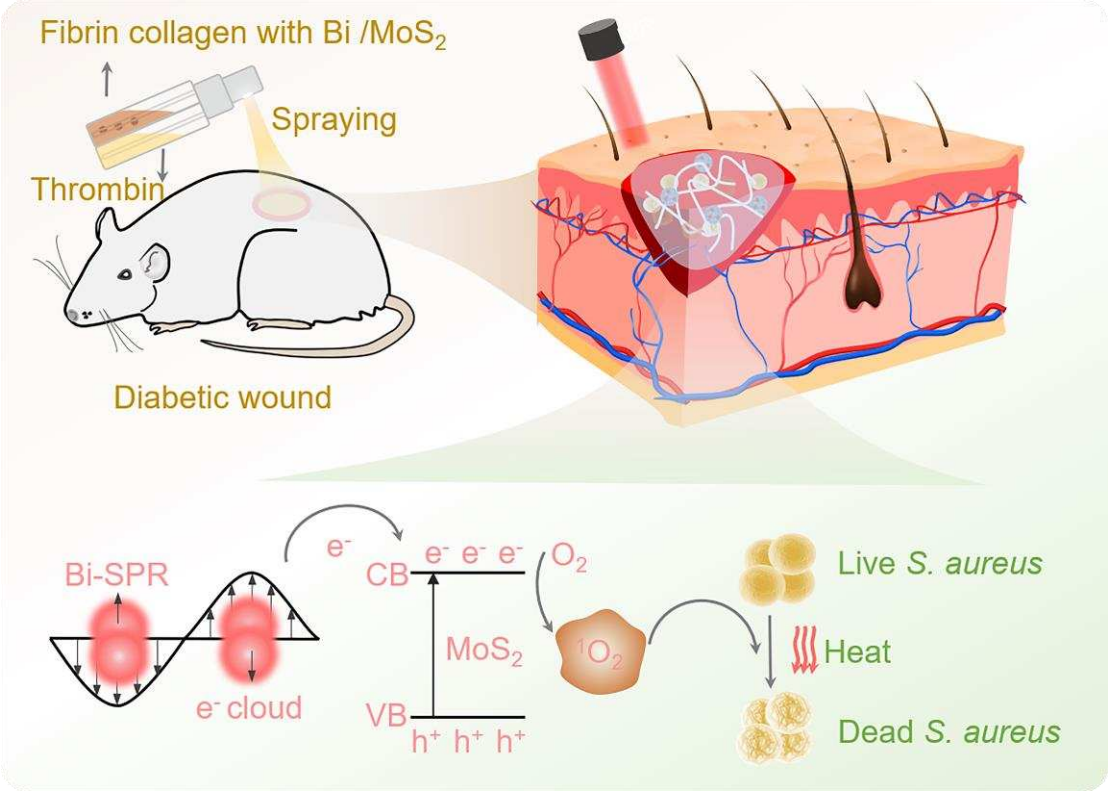

Scheme 1. Schematic illustration of Bi/MoS_2 heterojunction-doped in-situ sprayed composite hydrogel for LSPR-enhanced photocatalysis antibacterial, facilitating angiogenesis and accelerating diabetic wound healing.

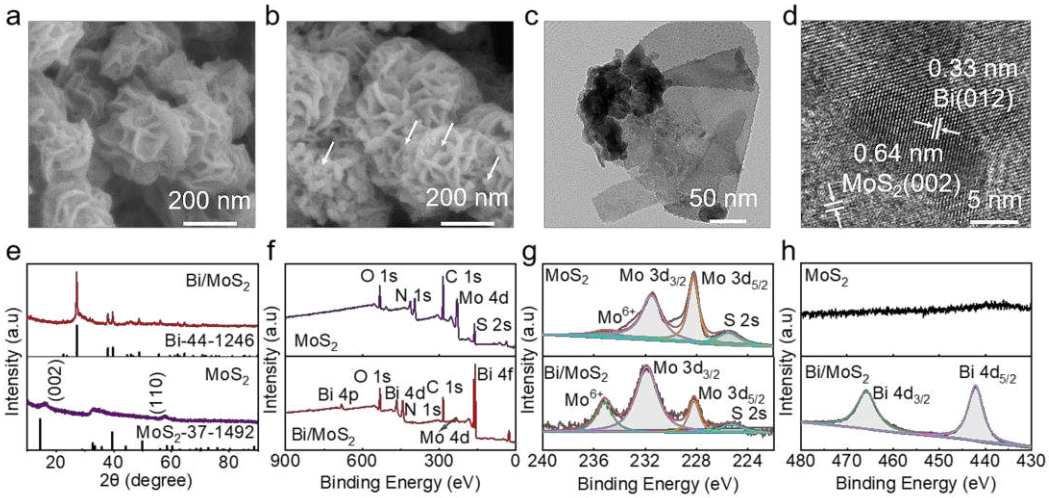

Fig. 1. Morphology and chemical composition characterization. (a) SEM image of MoS_2. (b) SEM image of Bi/MoS_2 composites. (c, d) HR-TEM image of Bi/MoS_2 composites. (e) XRD patterns. (f) XPS survey plot. (g, h) High-resolution XPS spectra of S, Mo and Bi.

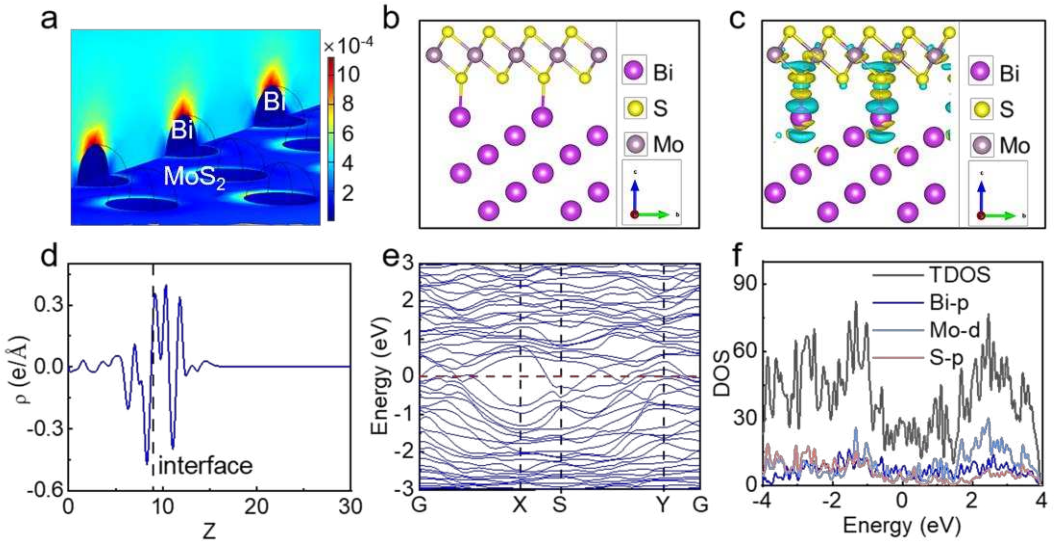

Fig. 2. The electromagnetic field distribution and the density-functional theory (DFT) calculations of as prepared Bi/MoS_2. (a) Electromagnetic field distribution of Bi/MoS_2 by COMSOL Multiphysics. (b) Simulated crystallographic structure. (c) Differential charge density map. (d) Plane-averaged differential charge density. (e, f) Band structure diagram and density of states of Bi/MoS_2 based Vienna Ab initio Simulation Package (VASP).

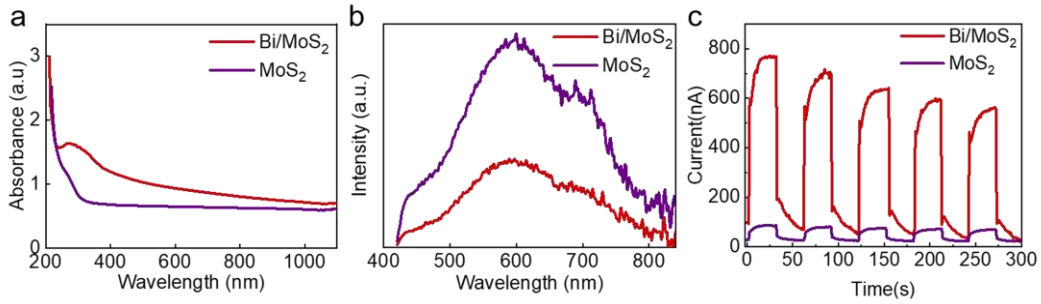

Fig. 3. Photoresponsive properties of Bi/MoS_2 heterojunction. (a) UV–vis-NIR spectra. (b) PL spectrum. (c) Transient photocurrent response.

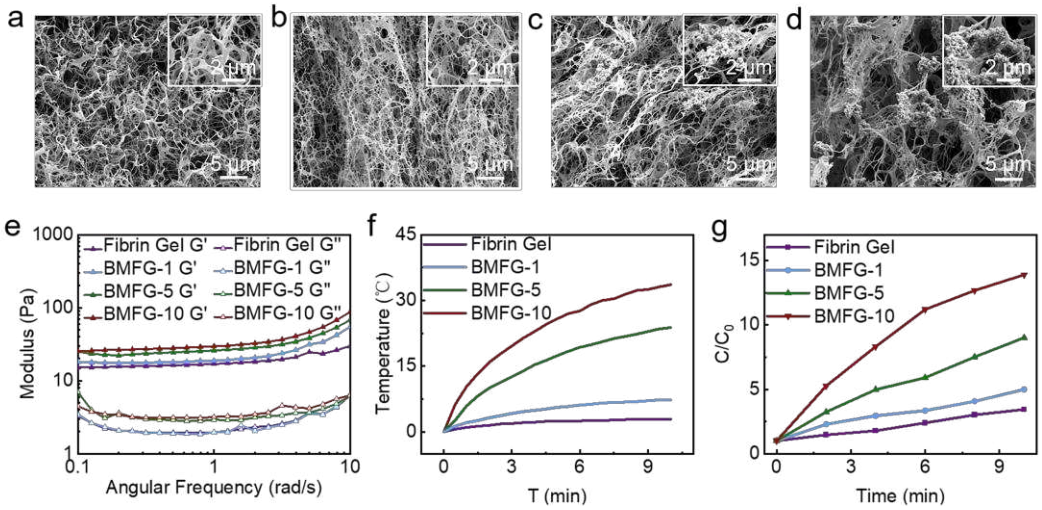

Fig. 4. Morphology and properties of composite gels. (a-d) Morphology of FG, BMFG-1, BMFG-5 and BMFG-10. (e) Rheological curve. (f) Photothermal heating curve of Bi/MoS_2 heterojunction-loaded fibrin gel. (g) ROS production of Bi/MoS_2 heterojunction-loaded fibrin gel under 808 nm irradiation as determined by DCFH.

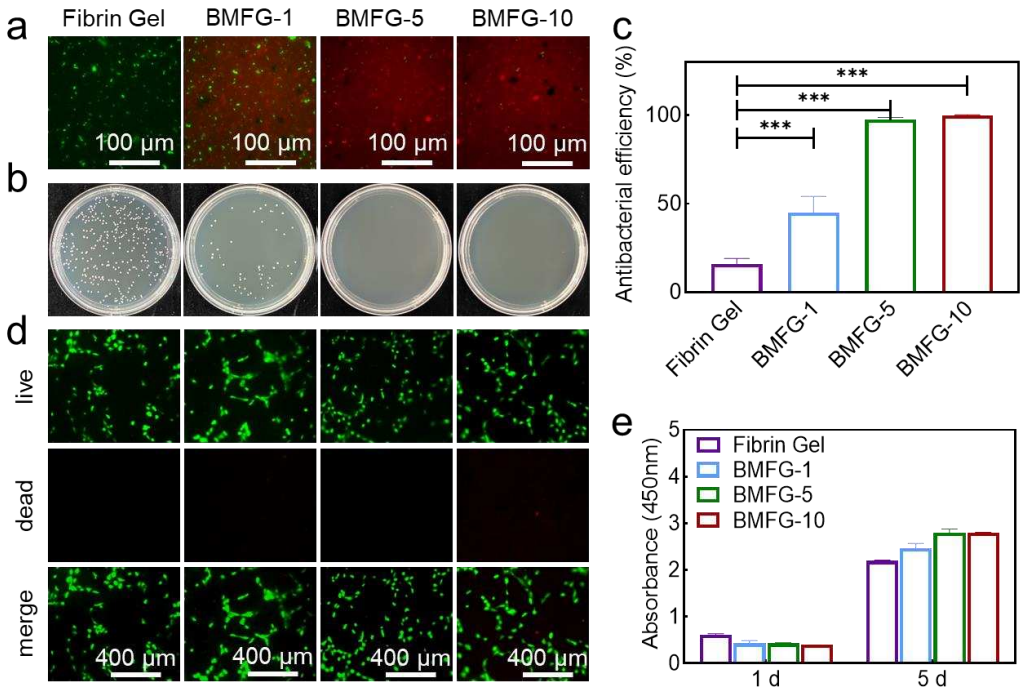

Fig. 5. Antibacterial effect against *S. aureus* and biocompatibility of Bi/MoS_2 heterojunction-loaded fibrin gel. (a) Bacterial dead/live fluorescent staining. (b) The colonies forming unit images. (c) The antibacterial ratios. (d) HUVECs dead/live fluorescent staining. (e) Quantitative determination of the cell viability. Mean ± SD, one-way ANOVA followed by Tukey's post hoc test for multiple comparison (***$p < 0.001$).

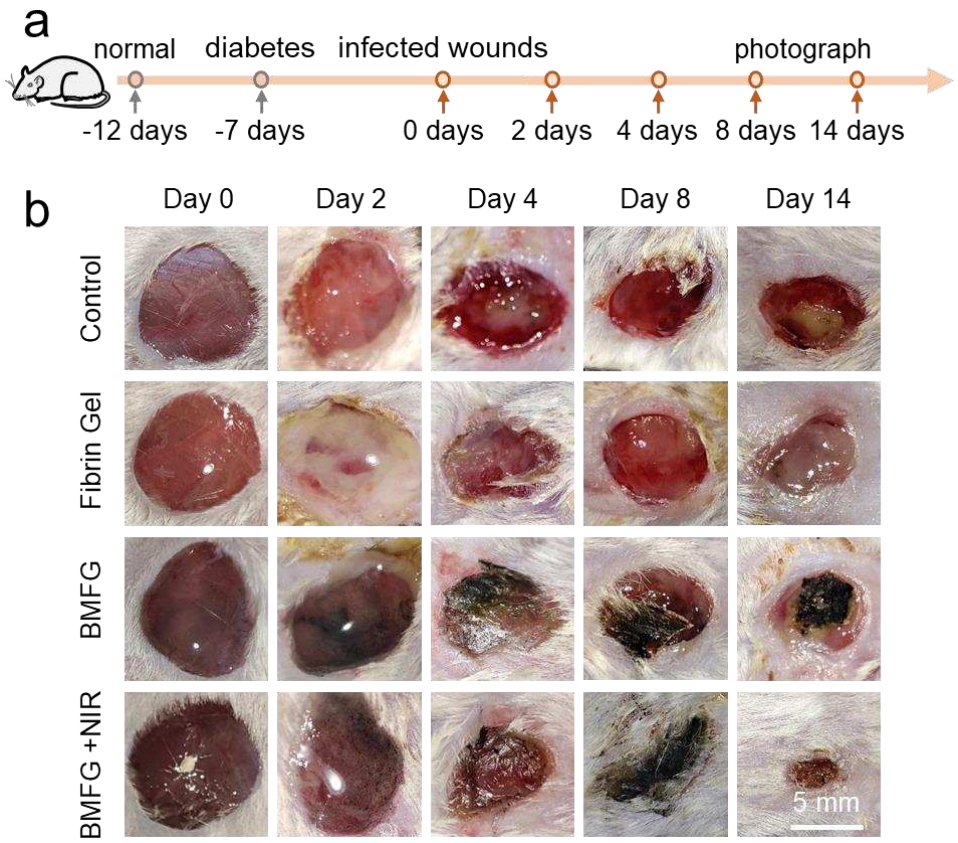

Fig. 6. *In vivo* study: treatment effects of *S. aureus*-induced wound infections with Bi/MoS_2 heterojunction-loaded fibrin gel. (a) The animal model of *S. aureus*-infected diabetic wounds. (b) The corresponding series of photographs showcased the progression of wound healing in mice at days 0, 2, 4, 8, and 14.

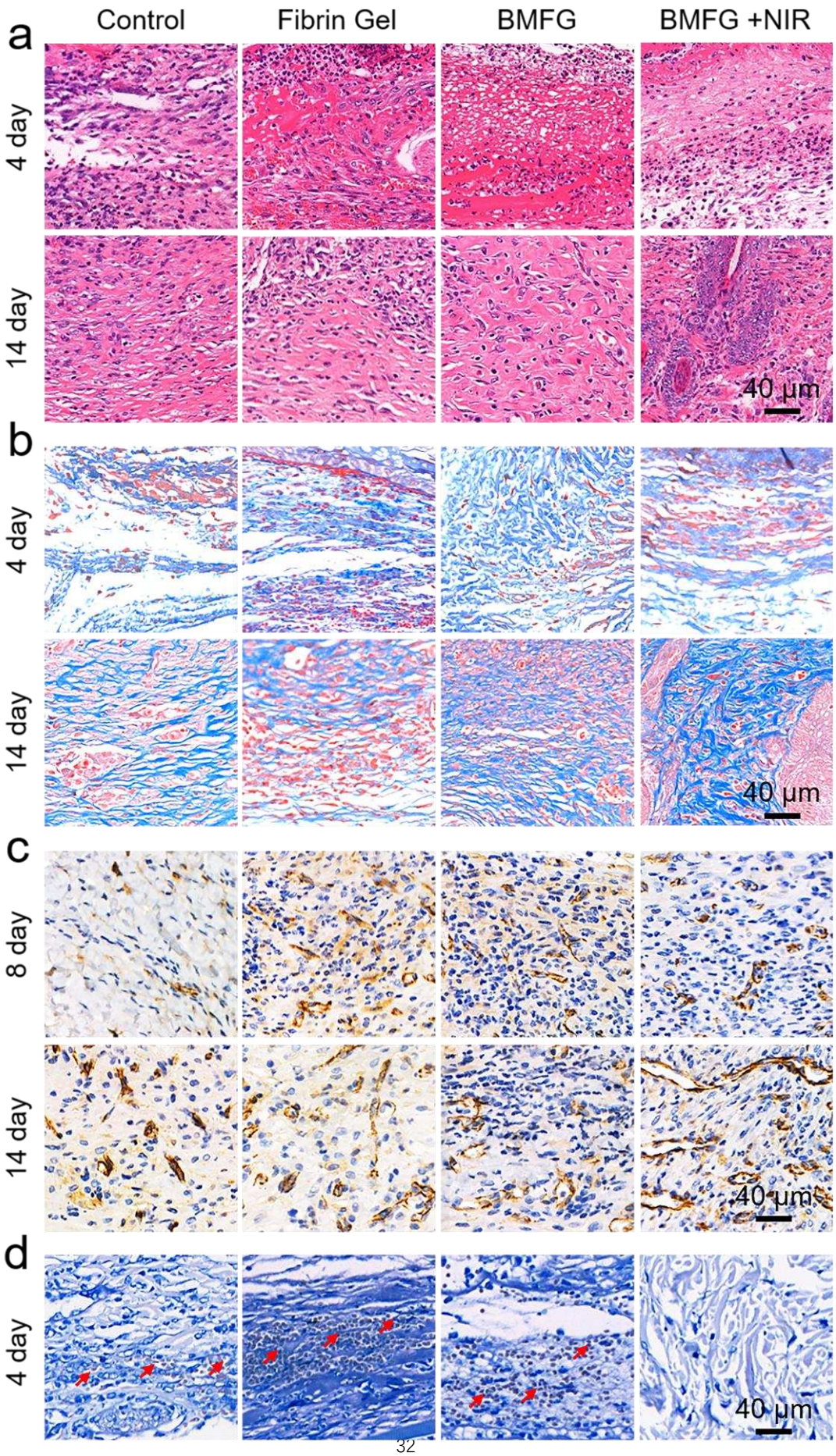
Control
Fibrin Gel
BMFG
BMFG +NIR
a
4 day
14 day
40 μm
b
4 day
14 day
40 μm
c
8 day
14 day
40 μm
d
4 day
40 μm

Fig. 7. Bi/MoS_2 heterojunction-loaded fibrin gel reduced inflammation, increased collagen deposition, promoted angiogenesis, and eliminated bacteria in diabetic mice. (a) H&E staining images for 4 days and 14 days. (b) Masson staining images for 4 days and 14 days. (c) CD31 staining images for 8 days and 14 days. (d) Giemsa staining images of wound regeneration skin on mice' wounds after treating with samples for 4 days.